



# Dynamic and synoptic study of spring dust storms over northern Saudi Arabia

Abdul-Wahab S. Mashat<sup>1</sup> · Adel M. Awad<sup>1</sup> · Mazen E. Assiri<sup>1</sup> · Abdulhaleem H. Labban<sup>1</sup>

Received: 6 February 2019 / Accepted: 6 January 2020 / Published online: 29 January 2020  
© Springer-Verlag GmbH Austria, part of Springer Nature 2020

## Abstract

The synoptic and dynamic characteristics of dust storm events over northern Saudi Arabia were studied during the spring season from 1978 to 2008 using surface dust storm observations from 11 stations and meteorological data from the NCEP/NCAR reanalysis dataset. Two-day dust-free periods were selected before and after each event to represent the pre- and post-event stages, respectively. The synoptic study identified two synoptic systems associated with dust events, i.e., frontal systems and shamal systems, and these systems were associated with increases in the pressure and temperature gradient over the northern Arabian Peninsula (AP) and an eastward shift in the maximum wind as a dust storm event progressed from the pre- to post-event stages. The dynamic study also showed that during the pre-event stage, the atmosphere was baroclinic and featured dynamic disturbances by frontal systems. Additionally, frontal systems resulted in slightly greater intensification than the shamal systems. Moreover, the dynamic study demonstrated that the kinetic energy (KE) shifted eastward and the available potential energy (APE) shifted northward through a series of regions importing and exporting KE and APE. The vertical profile of the average energy area indicated that the main layer in which sensible heat was converted into KE was located above the dust cloud.

## 1 Introduction

The Saharan area and the deserts of the Arabian Peninsula (AP), Iraq, and Syria represent major natural sources of dust hazards affecting Africa, Southwest Asia, and the Middle East (Middleton 1986; Prospero et al. 2002; Washington et al., 2003; Natsagdory et al. 2003; Hamidi et al. 2013) and are major sources of global dust, as shown by Pease et al. (1998). The dust emissions from the AP and Middle East deserts have been estimated to represent approximately 20% of the total global dust emissions, based on the average emissions mentioned in Ginoux et al. (2004).

Specifically, northern Saudi Arabia has been classified as a temporary dust source area over the AP, as detected by Mashat and Awad (2010), and is considered a region of cyclolysis resulting in spring Saharan cyclones, as indicated by Hannachi et al. (2011). In addition, Notaro et al. (2013) identified the Sahara Desert as a primary remote dust source for western and northern Saudi Arabia and identified the Iraqi and

Syrian deserts as the primary local dust sources for northern and eastern Saudi Arabia.

The release of dust from sources in the Sahara, AP and Middle East is frequently observed in summer (Smirnov et al. 2002; Goudie and Middleton 2006) and spring (Kaskaoutis et al. 2008; Ginoux et al. 2012; Yu et al. 2013; Awad and Mashat 2014a; Rashki et al. 2014). However, appropriate atmospheric conditions are needed to release and transfer dust from its sources, as described by Goudie and Middleton (2006). Therefore, analyses of the synoptic features and identification of their characteristics are important for evaluating different synoptic dust regimes and their development, as found in Natsagdory et al. (2003) and Awad and Mashat (2014a). Accordingly, the dust concentrations in the regions downwind of the dust sources are greatly influenced by synoptic conditions (Alpert et al. 2004a; Ganor et al. 2010; Awad and Mashat 2014b, 2016a).

To identify the synoptic systems responsible for dust events, Engelstaedter et al. (2006) explained the annual dust cycle over Africa according to seasonal changes in the inter-tropical convergence zone and the associated rainfall, while Washington and Todd (2005) incorporated the strength of the low-level jet as an additional factor. Additionally, Raispaur et al. (2014) found that the polar jet stream affected more than 20% of the total dust events in southwestern Iran during the cold season. Furthermore, Shalaby et al. (2015) demonstrated

✉ Adel M. Awad  
awad\_adel@yahoo.com

<sup>1</sup> Department of Meteorology, King Abdulaziz University, Jeddah, Saudi Arabia

that in winter and early spring (January–April), AP dust is influenced by the extension of the Siberian high-pressure system over the northern AP and the Red Sea trough over the southern AP, and they described the importance of the dominant anticyclonic wind field over the AP during dust events. Al-Jumaily and Ibrahim (2013) showed that Iraq dust is controlled by the low-pressure system over Iran and by shamal (northerly) winds and the associated instability. Amanollahi et al. (2015) discussed the effect of the temperature contrast between the Mediterranean Sea and the Syrian Desert on the occurrence and amount of dust over western Iran. Moreover, Hamidi et al. (2013) identified shamal and frontal dust storms as the two primary dust storm categories in the Middle East. Shamal dust storms are produced by the interaction between the Mediterranean high-pressure and southern Iran low-pressure systems, while frontal dust storms are produced by the interaction between the southern Iran high-pressure and eastern Mediterranean low-pressure systems.

To determine the relationships among different dust sources, Mohalfi et al. (1998) and Awad and Mashat (2014b) demonstrated the influence of the pressure gradient between the Azores high-pressure system and the thermal low-pressure system located over the AP on the transport of dust from northeastern Africa to Asia and on Mediterranean dust episodes, which was also investigated by Gkikas et al. (2012). In addition, Vishkaee et al. (2011) found that dust storms are essentially triggered by the dynamic lifting of cold fronts and their associated midlatitude troughs during the winter and by the lifting of the vertical mixing produced by solar heating during summer. In general, frontal passages, which have strong winds associated with intense baroclinicity, are frequently considered a trigger mechanism of dust storms, as indicated by Hamidi (2019).

Kaskaoutis et al. (2016) defined the Caspian Sea–Hindu Kush Index (CasHKI), which is a meteorology-climatology index, as the difference between the spatially averaged mean sea level pressure (MSLP) anomalies over the Caspian Sea (CS) and Hindu-Kush (HK), and concluded that the index was related to dynamic atmospheric changes. Furthermore, Kaskaoutis et al. (2017) indicated that a high CasHKI was accompanied by intensified northerly wind, which led to an increase in dust over eastern Iran. In their analysis of cyclonic Mediterranean system energy (which represents a transit stage in the influence of Saharan dust on northern Saudi Arabia), Abdel Wahab and Abdel Basset (2000) indicated that horizontal flux convergence represented the main source of energy, while the generation of kinetic energy (KE) via cross-contour flux was the main sink of KE, except during the decay stage.

The previous dynamic analyses in studies on dust events are insufficient to provide detailed insights into dust events; therefore, this study focused on studying the dynamics of dust events using the relationship between the energy and synoptic factors in the atmosphere leading

up to and during the production of dust events. In addition, we evaluated the changes in the regional atmosphere after the passing of a dust event.

This paper is organized as follows. Section 2 describes the data and methodology used. Section 3 provides the synoptic results related to the dust storm event stages and the associated dynamic characteristics. Section 4 discusses the results of the synoptic and dynamic features of the dust storm event stages and presents the conclusions of the study.

## 2 Data and methodology

Observations of dust intensity were retrieved from 11 surface meteorological stations over northern Saudi Arabia (Fig. 1a). In this study, the different dust/sand storms (WMO codes (WW) 09 or 30–32) and severe dust/sand storms (WMO codes (WW) 33–35) that were observed at the surface stations were classified into a single category called dust storms (WMO, 2005). Additionally, meteorological data with a spatial resolution of  $2.5^\circ \times 2.5^\circ$  were derived from the National Center for Environmental Prediction and the National Center for Atmospheric Research (NCEP/NCAR) reanalysis for synoptic and dynamic studies, as described by Kalnay et al. (1996) and Kistler et al. (2001).

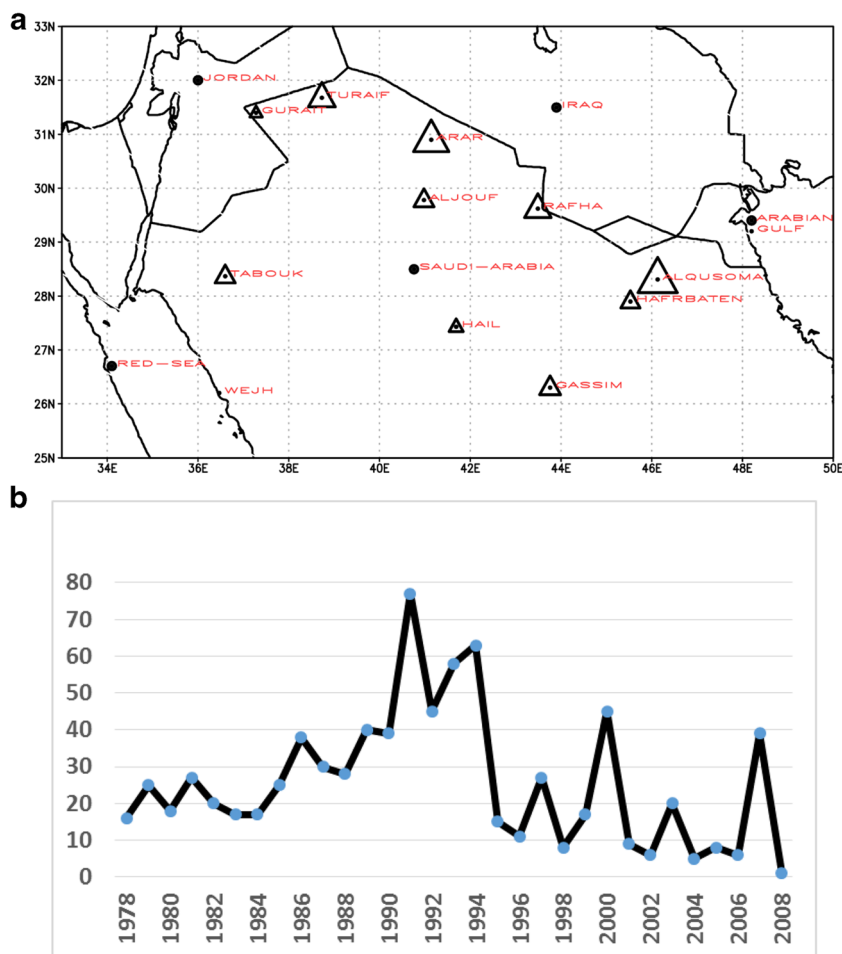
The dust storm events were selected under the following conditions:

- 1- A dust event was defined based on the number of continuous days with observed dust storms at one or more stations in northern Saudi Arabia.
- 2- For each dust event selected in this study, there were at least 2 days before and after the event time in which no station observed dust storms. Thus, the dust storm event is referred to as the event stage; the 2-day period before the event is referred to as the pre-event stage; and the 2-day period after the event is referred to as the post-event stage.

The meteorological data at 12 GMT (corresponding to the closest time of active dust) from 1978 to 2008 were used to study the synoptic features during the spring season. These data consist of the MSLP, the geopotential height and horizontal wind components at 850 hPa and 500 hPa, the maximum wind at 250 hPa, the temperature at 850 hPa, and the static stability using the formula from Gates (1961) in the layer between the pressure levels of 1000 and 500 hPa. In addition, maps of deviations from the climatology for each parameter were prepared for the different dust storm event stages.

The energy equations used are those from Smith (1969; Smith and Horn 1969; Prezerakos and Michaclides 1989), and these equations represent the regional changes in KE and available potential energy (APE) and their

**Fig. 1** **a** Average distribution of dust storms (triangles) across the weather stations. The sizes of the triangles represent the relative number of observed dust storms, and the black circle represents the closed countries or the main water areas. **b** Annual distribution of dust storms



relationship with one another and with global energy (Lorenz 1955; Danard, 1966; Chen and Lee 1983).

$$\frac{\partial K}{\partial t} = - \left[ \nabla \cdot \mathbf{V}K + \frac{\partial}{\partial p} \omega K \right] - \left[ \nabla \cdot \mathbf{V}\Phi + \frac{\partial}{\partial p} \omega \Phi \right] - \alpha\omega - \mathbf{V} \cdot \mathbf{F} \quad (1)$$

$$\frac{\partial A}{\partial t} = - \left[ \nabla \cdot \mathbf{V}A + \frac{\partial}{\partial p} \omega A \right] + \alpha\omega + Q \quad (2)$$

where  $A = c_p \frac{p^* - p_s^*}{p^*} T$  is the APE.

The left side of Eq. 1 ( $\frac{\partial K}{\partial t}$ ) represents the time change for KE. The first term ( $-\left[ \nabla \cdot \mathbf{V}K + \frac{\partial}{\partial p} \omega K \right]$ ) on the right side represents the flux convergence (horizontal and vertical) of KE, the second term ( $-\left[ \nabla \cdot \mathbf{V}\Phi + \frac{\partial}{\partial p} \omega \Phi \right]$ ) represents the generation of KE via cross contours (GKE), the third term ( $-\alpha\omega$ ) represents the conversion of sensible heat (SH) into KE or vice versa, and the last term ( $-\mathbf{V} \cdot \mathbf{F}$ ) represents the dissipation of KE.

The left side of Eq. 2 ( $\frac{\partial A}{\partial t}$ ) represents the time change for APE. On the right side, the first term ( $-\left[ \nabla \cdot \mathbf{V}A + \frac{\partial}{\partial p} \omega A \right]$ ) represents the flux convergence (horizontal and vertical) of APE, the second term ( $+\alpha\omega$ ) represents the conversion of

KE into SH or vice versa, and the last term ( $Q$ ) represents the dissipation of APE or the rate of heating (RH).

The dynamic structure behind the development of these dust events was investigated using 6 hourly meteorological data and the energy budget terms of KE and APE, as has been done in previous balance equations. The result of the dynamic part depended on the area average, zonal vertical cross section, and horizontal vertical average. The area average included the terms, the conversion of SH into KE, the vertical flux convergence of KE (VKE), the vertical flux convergence of APE (VAP), and the GKE. The zonal vertical cross section of the meridional average content, the KE and RH, and the horizontal distribution of the vertical average contents are the horizontal flux convergence of KE (HKE) and APE (HPE). The area average was confined to 20–35 °N and 20–40 °E, which represents the effective dust storm area over northern Saudi Arabia, as shown in Fig. 1a. The units of energy, from its definition using the meter-kilogram-second (MKS) system of units, were measured in watts per square meter, except for KE, which was measured in joules per square meter.

This study defined the synoptic and dynamic characteristics of dust storms via the following steps:

- 1- Compare the characteristics of composite event stages with the spring climatology composite to determine how much the atmospheric dust stages differ from the regional climatology.
- 2- Compare the characteristics of each event stage with the characteristics of the pre-event and post-event stages to determine how much these characteristics changed through the different event stages. These comparisons were used to determine the favorable conditions that prepare the atmosphere to produce a dust event and help identify how much the dust event conditions change after the dust storm moves out of a region.

## 3 Results

### 3.1 Ground-based measurement variability

The distribution of dust storms (triangles) shown in Fig. 1a shows that the ALQUSOMA station has the highest number of observed dust storms with 133 observations, while the WEJH station has the lowest number of observed dust storms with 4 observations. Generally, the WEJH, GURAIAT, ALJOUF, TABOUK, HAIL, GASSIM, and HAFRBATEN stations experience fewer dust storms than the mean number of all stations (72.7 observations/season). In contrast, the TURAIF, ARAR, RAFHA, and ALQUSOMA stations experience more dust storms than the mean value. Furthermore, the distribution shows that the stations along the eastern boundary have the highest number of dust storms, while the central stations have a relatively low number of dust storms.

The monthly average distributions of “dust” and “severe dust” storms for all stations (Table 1) show that the number of observations increases from March to May, i.e., increasing into the warmer months. In addition, the distribution shows that the number of severe dust storm observations is less than the number of dust storm observations, representing a proportion of approximately 50%.

The annual distribution of dust storms, as shown in Fig. 1b, shows an increasing trend in the total number of observations from 1978 to 1994 and a gradually decreasing trend from 1995 to 2008. Moreover, the absolute

**Table 1** Monthly average distributions of dust storms and severe dust storms observed at all surface stations in northern Saudi Arabia

Month/phenomena	Dust storm	Severe dust storm
March	7.2	3.6
April	8.7	4.2
May	9.9	4.9

decreasing rate in the second period is less than the absolute increasing rate in the first period.

### 3.2 Synoptic climate patterns

To describe the synoptic features of the dust storm events, the spring climatological situations were first described, and then the changes in the event stages were evaluated and compared with the climate conditions.

#### 3.2.1 MSLP and maximum wind at 250 hPa

The map of the climate in the spring season from 1978 to 2008 (Fig. 2a) shows that the southern AP was affected by a low-pressure cell, with a pressure of 1007 hPa, which appeared as an extension from the Indian monsoon low. In addition, in association with the Sudan low, the southern low-pressure cell formed a deep trough over the eastern Red Sea, as described by Awad and Almazroui (2016b) and Awad and Mashat (2018), and a weak-gradient trough over the western Arabian Gulf, which extended northward to Turkey. Moreover, the Azores High, with a pressure of 1018 hPa, formed a deep ridge over the Mediterranean and northwestern AP and an area with a high-pressure gradient over the eastern Mediterranean, Levant and northwestern AP. Furthermore, the Siberian high-pressure system, with a pressure of 1020 hPa, formed a ridge that extended westward over the Caspian and Black Seas and a short weak ridge over the Arabian Gulf.

The maximum wind at 250 hPa, as shown in Fig. 2a, had a core that extended from Libya to the eastern AP, with a maximum value of 98 knots. In addition, the maximum wind formed a trough over the northern Red Sea and a ridge over the northern AP.

In the pre-event stage, as shown in Fig. 2b, the Azores High experienced an increase in pressure to values greater than 1.0 hPa, and it shrank westward. The Siberian High and its ridge over the Arabian Gulf strengthened, and the pressure increased by more than 0.5 hPa; however, the pressure over the eastern Sahara and Mediterranean regions decreased by more than 1.0 hPa. Additionally, the maximum wind had a core that extended from Algeria to the mid-northern AP and had a maximum value of 106 knots.

In the event stage, as shown in Fig. 2c, the Azores High strengthened, the pressure increased by more than 0.5 hPa, and the high-pressure system extended eastward. The Siberian High weakened and shrank eastward. However, the low-pressure system and trough over the AP and eastern Mediterranean regions deepened to more than 2.5 hPa. The core of the maximum wind, as shown in Fig. 2c, extended from western Africa to the eastern AP, and the maximum value reached 109 knots. In addition, the core shifted southward relative to the climatological position.

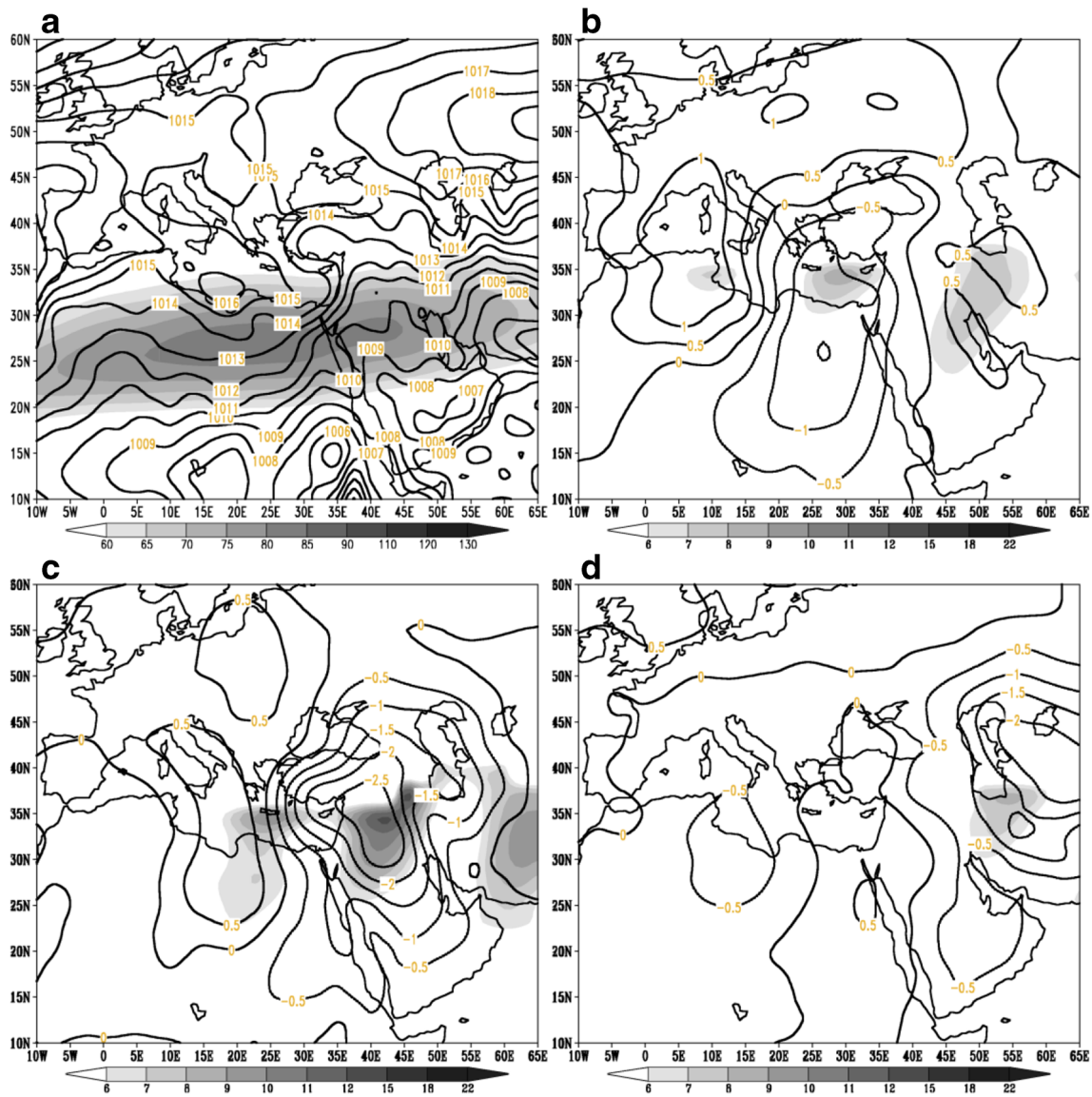


**Fig. 2** The composite maps of the MSLP (isobars, in hPa) and maximum wind at 250 hPa (shading, in knots) for **a** the spring season from 1978 to 2008 and the deviations **b** 2 days before a dust storm event, **c** during the event, and **d** 2 days after the event

In the post-event stage, as shown in Fig. 2d, the Azores High weakened by more than 0.5 hPa, and the Siberian High and its ridge over the eastern AP weakened by more than 2.0 hPa. Additionally, the low pressure around the Red Sea increased by more than 0.5 hPa. The core position of the maximum wind, as shown in Fig. 2d, shifted eastward and extended from Tunisia to western Iran; its maximum value reached 107 knots, and its position shifted southward relative to its climatological position.

### 3.2.2 Geopotential height, wind, and temperature at 850 hPa

The climate map in Fig. 3a shows that the northern cyclone, with a value of 1380 gpm, had a deep trough over the eastern Mediterranean, Levant and northern AP. The subtropical

anticyclone, with a value of 1530 gpm, had a ridge extending from Africa to the western Red Sea. In addition, an anticyclonic cell with a value of 1510 gpm was located over the eastern AP (known as the Arabian anticyclone, Raziei et al. 2012; De Vries et al. 2013; Awad and Mashat 2016a) and, in conjunction with the cyclone over Pakistan, reached 1470 gpm and formed a geopotential gradient over the Arabian Gulf. Additionally, an area of geopotential gradient over northern Sahara and the Mediterranean formed between the northern cyclone and subtropical anticyclone over Africa.

The distribution of climatological temperature, as shown in Fig. 3a, shows a high-temperature cell (greater than 26 °C) located over the southern AP and forming a high-temperature ridge over the northern AP. Moreover, the high-temperature cell over the AP formed a strip-shaped zone with a

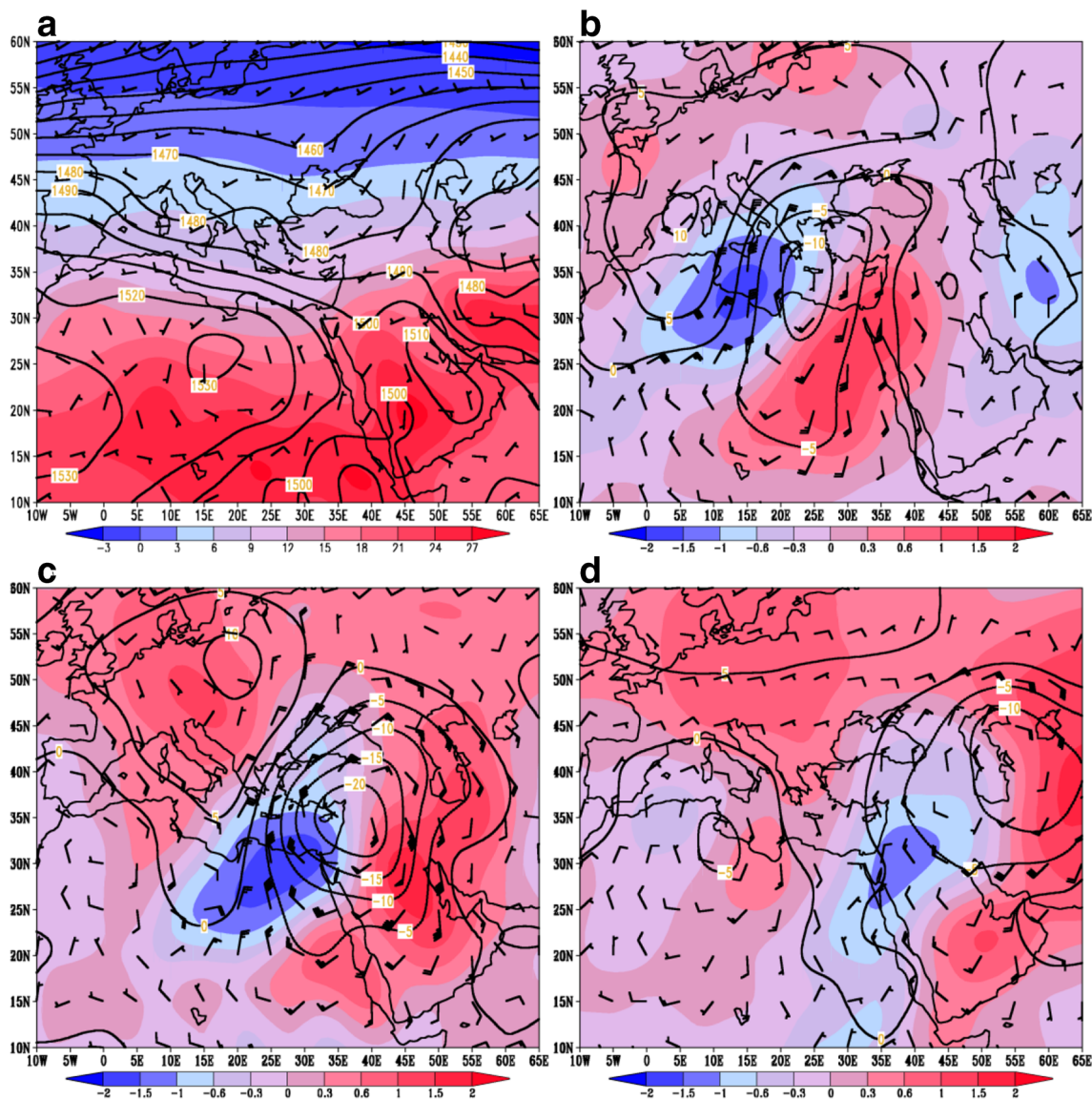


**Fig. 3** The composite maps of the geopotential height (contours, in gpm), wind (barbs, in knots), and temperature (shading, in °C) at 850 hPa for **a** the spring season from 1978 to 2008 and the deviations **b** 2 days before a dust storm event, **c** during the event, and **d** 2 days after the event

temperature gradient with the surrounding temperatures over the Red Sea and over the eastern and northern parts of the AP. Generally, the temperature distribution exhibited a more pronounced gradient to the south of 45 °N than to the north of 45 °N. In addition, the wind distribution formed an anticyclonic wind pattern over the eastern AP and a cyclonic wind pattern over the western AP.

In the pre-event stage composite, as shown in Fig. 3b, the anticyclonic cell over the eastern AP strengthened, and the highest geopotential increased by at least 4.0 gpm. However, the geopotential over eastern Africa decreased by approximately 10 gpm, which formed favorable conditions for increasing the geopotential gradient area over the western AP, eastern Mediterranean and Levant. In addition, the change in the geopotential increased the anticyclonic

wind over Iraq and the northeastern AP and produced convergent winds over the western AP while decreasing the eastern wind over the northern AP.

In the event stage, as shown in Fig. 3c, the geopotential over the northern AP decreased by more than 24 gpm, and the geopotential decreased over the entire AP, eastern Africa and eastern Mediterranean regions. Furthermore, the northern cyclone trough over Europe weakened, and the geopotential height increased by more than 10 gpm. These developments tended to change the wind over the northern AP and the surrounding area into a cyclonic wind pattern, with the maximum value over the northern AP.

In the post-event stage, as shown in Fig. 3d, the geopotential center decreased, similar to the pattern in the previous stage, by more than 12 gpm and shifted eastward

over the CS. Additionally, the geopotential increase over Europe shifted northward and exceeded 8.0 gpm. In addition, a new geopotential decreasing area was generated over northern Africa, i.e., over Algeria, with decreases in the areas with values greater than 4.0 gpm. These developments tended to decrease the wind over the AP compared with the previous event stages and changed the wind direction over the northern AP from west to northwest.

### 3.2.3 Geopotential height and wind at 500 hPa and static stability of the 1000–500-hPa layer

The climate map at 500 hPa in Fig. 4a shows that the northern cyclone, with a value of 5480 gpm, had a deep trough over the eastern Mediterranean and eastern Africa, while the subtropical anticyclone, with a value of 5880 gpm, had two ridges: one over central Africa and the Mediterranean, and one over the AP and northern Iran. In addition, high wind speeds were observed over the Mediterranean, northern Africa and northern AP, and reduced wind speeds were observed over the northern and southern regions.

The climate static stability (Fig. 4a) shows that a weak stable area runs from south to north in the middle of the AP, with values of 0.35 deg db<sup>-1</sup> over the northern region and 0.4 deg db<sup>-1</sup> over the southern region; however, this region is surrounded by relatively highly stable areas to the west and east. In addition, the distribution of the stability indicated a highly stable area over the Mediterranean, and the highest value of 0.9 deg db<sup>-1</sup> was detected over the central Mediterranean. The Saharan region had the lowest value of 0.45 deg db<sup>-1</sup> over central Sahara. Generally, the distribution of stability forms a high-stability gradient over the western AP, southern Mediterranean, or northern Saharan region and over the Levant area. Furthermore, a small area of high stability, with a value of 0.6 deg db<sup>-1</sup>, was located over the Arabian Gulf and formed a relatively high-gradient strip over the western Arabian Gulf.

In the pre-event stage, as shown in Fig. 4b, the trough over eastern Africa and the Mediterranean deepened by more than 25 gpm, while the ridge over the AP strengthened by more than 10 gpm. This change in the atmospheric system tended to generate an anticyclonic wind pattern over the AP and formed a geopotential gradient over the eastern Mediterranean region.

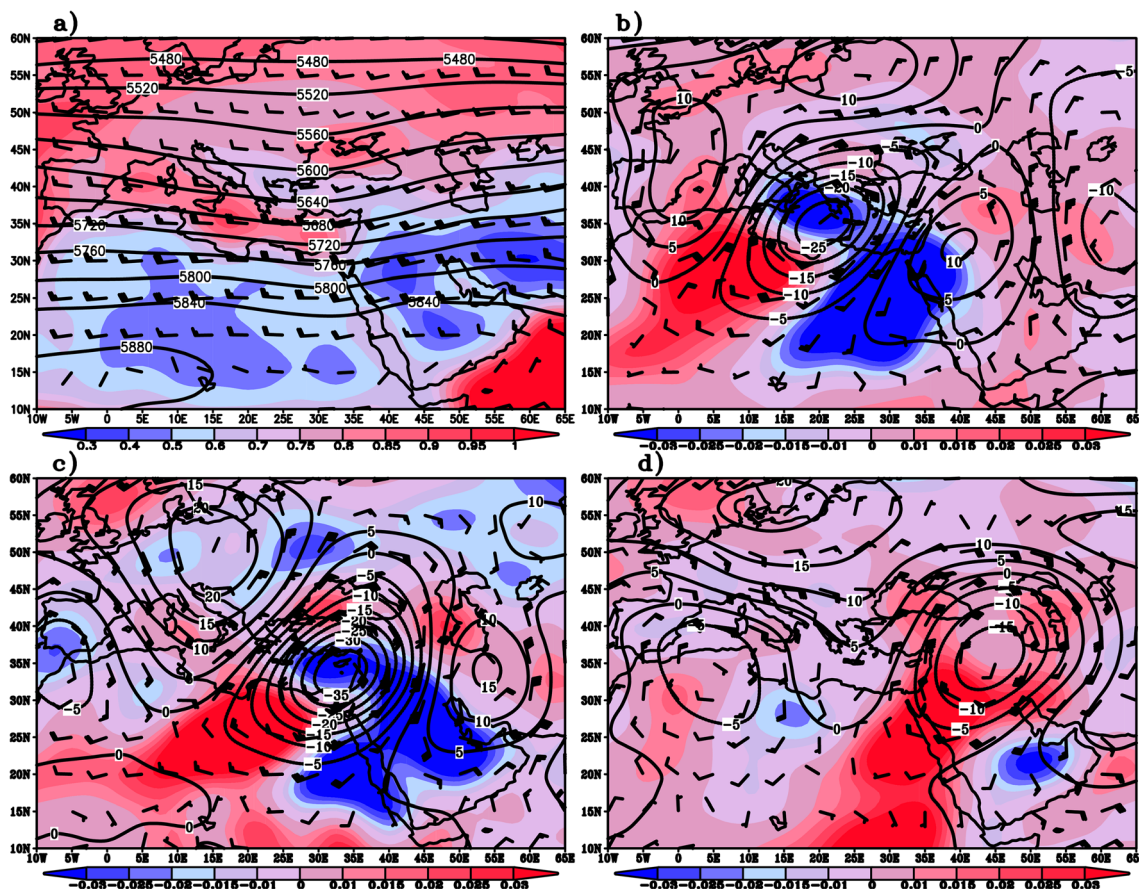


**Fig. 4** The composite maps of the geopotential height (contours, in gpm), wind (barbs, in knots) at 500 hPa, and static stability (shading, in deg db<sup>-1</sup>) of the layer between 1000 and 500 hPa for **a** the spring

season from 1978 to 2008 and the deviations **b** 2 days before a dust storm event, **c** during the event, and **d** 2 days after the event

The static stability differences from the climatological situation, as shown in Fig. 4b, formed two areas with opposite differences. The first area had a negative difference, or decreased stability, over eastern Africa and the Mediterranean, with the highest decreasing rates of  $-0.07 \text{ deg db}^{-1}$  over Egypt and  $-0.04 \text{ deg db}^{-1}$  over the central Mediterranean. The second area had a positive difference, or increased stability, over western Africa, with a maximum increase of  $0.04 \text{ deg db}^{-1}$  over Algeria. Furthermore, the eastern AP exhibited increased stability, with a small increase of approximately  $0.01 \text{ deg db}^{-1}$  over the southern region.

In the event stage, as shown in Fig. 4c, the deepening of the northern trough increased by more than 35 gpm, and the trough shifted eastward. Additionally, the strength of the ridge increased by more than 15 gpm. As a result of this development, the geopotential gradient over the eastern Mediterranean region increased, and a cyclonic wind pattern formed over the region, while the anticyclonic wind pattern that appeared in the pre-event stage shifted eastward to central Iran.

The static stability, as shown in Fig. 4c, indicated that the two distinct areas in the previous stage shifted eastward, and the area of lower stability was located over the AP and eastern Mediterranean. Specifically, the highest difference of  $-0.05 \text{ deg db}^{-1}$  was located over the eastern region, and the area of high stability was located over Libya and Egypt, with the highest difference of  $0.06 \text{ deg db}^{-1}$  over Libya.

In the post-event stage, as shown in Fig. 4d, the northern trough appeared to be filled, and the geopotential increased by more than 5.0 gpm; additionally, the ridge over the AP weakened, and the geopotential decreased by more than 15 gpm. As a result of this development, a weak cyclonic wind pattern formed and influenced the region, and the geopotential gradient decreased.

The static stability, as shown in Fig. 4d, indicated that the distinct areas shown in the previous stages shifted eastward, and the highly stable area moved over Egypt, the northern AP, and the Levant. Specifically, the highest difference of  $0.05 \text{ deg db}^{-1}$  was found over the northwestern AP, and the area of low stability shifted southeastward to the southern AP, with the highest difference of  $-0.03 \text{ deg db}^{-1}$ .

### 3.3 Dynamic climate study

#### 3.3.1 Vertical profiles

**CSK term ( $-\alpha\omega$ )** The climatological vertical distribution of the average conversion from SH to KE (CSK) throughout the area, as shown by the black line in Fig. 5a, indicated that in spring, the study area has a positive surface average CSK value of  $6.4 \times 10^{-2} \text{ W/m}^2$ , which indicates that the sinking of cold air and rising of warm air occur in this region (Margules 1903; Lorenz 1955; Kung 1966; Prezerakos and

Michaélides, 1989). In addition, the distribution shows that the maximum conversion from SH to KE occurs in the lower layer and decreases with height to approximately 700 hPa, with a value of  $1 \times 10^{-2} \text{ W/m}^2$ , and then increases slightly with height to 400 hPa, with a value of  $1.1 \times 10^{-2} \text{ W/m}^2$ . Above 250 hPa, the conversion decreases to negative values, reaching a minimum value of  $-4 \times 10^{-2} \text{ W/m}^2$  at 100 hPa, corresponding to the conversion of KE to SH.

The same distribution occurs in the pre-event situation, as illustrated by the red line in Fig. 5a, except that the magnitude of the conversion is slightly larger than that of the climatological pattern, reaching  $1.9 \times 10^{-2} \text{ W/m}^2$  at 300 hPa and negative values starting at 200 hPa, with a minimum value of  $-3.7 \times 10^{-2} \text{ W/m}^2$  at 100 hPa.

In the event situation, shown by the green line in Fig. 5a, the magnitude of the conversion is large, with a maximum value of  $7.9 \times 10^{-2} \text{ W/m}^2$  in the upper layer at 400 hPa, and negative values that start at 150 hPa, with a minimum value of  $-4.2 \times 10^{-2} \text{ W/m}^2$  at 100 hPa. This CSK profile is similar to the profile of the deepening phase of intensive cyclonic activity in the Mediterranean, as described by Prezerakos and Michaélides (1989). Furthermore, compared with the climatological situation, the magnitude of the conversion is seven times larger at 400 hPa and approximately two times larger at 850 hPa.

In the post-event situation, as shown by the blue line in Fig. 5a, the distribution of the vertical conversion appeared to be different. The conversion became negative above 700 hPa, decreasing from a value of  $0.2 \times 10^{-2} \text{ W/m}^2$  at 700 hPa to a negative value of  $-4.3 \times 10^{-2} \text{ W/m}^2$  at 100 hPa.

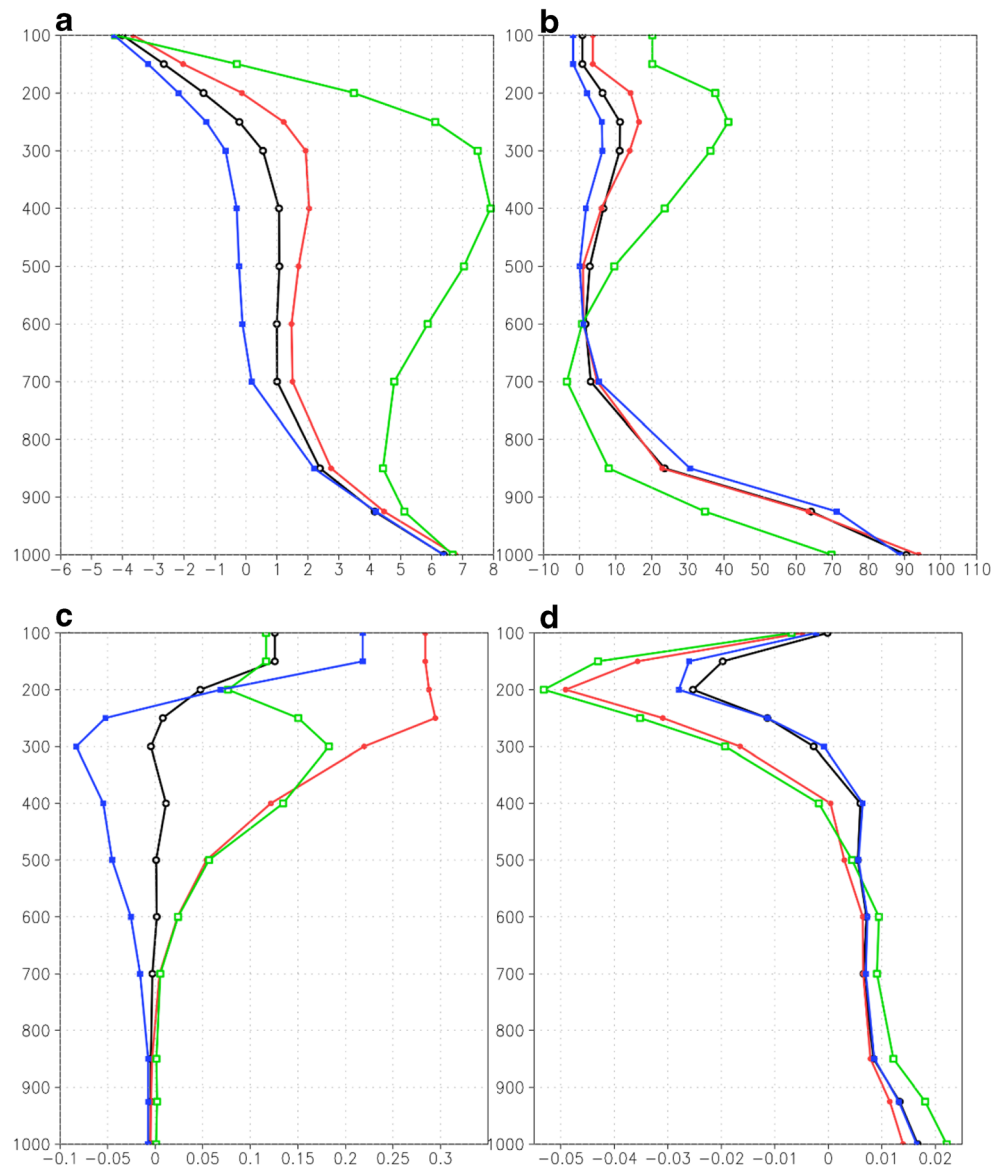
**Vertical flux convergence of APE (VAP) ( $-\frac{\partial}{\partial p}\omega A$ )** The vertical distribution of the climatological vertical flux convergence of APE (VAP) over the area, as shown by the black line in Fig. 5b, indicates that the climatological atmosphere featured a vertical import of APE at all levels, but two trends were observed in the rates. The first trend was characterized by a steep decreasing rate from the maximum magnitude at the surface of  $90.5 \times 10^{-2} \text{ W/m}^2$  to a value of  $1.6 \times 10^{-2} \text{ W/m}^2$  at approximately 600 hPa. The second trend was characterized by a slightly increasing rate from 600 to 250 hPa, with a value of  $11.2 \times 10^{-2} \text{ W/m}^2$ . The current lower layer of the maximum vertical import of APE is not pronounced in the general midlatitude cyclonic disturbances found by Kung and Baker (1975).

The same situation is observed during the pre-event stage, as shown by the red line in Fig. 5b; however, this distribution reached its minimum value at 500 hPa, with a value of  $1.0 \times 10^{-2} \text{ W/m}^2$ , and more vertical import of APE occurred in the upper layers above 400 hPa, with a maximum value of  $16.5 \times 10^{-2} \text{ W/m}^2$  at 250 hPa.

The situation is different for the event stage, as shown by the green line in Fig. 5b; the maximum value at the surface,



**Fig. 5** Vertical profiles of the area average terms of **a** conversion between KE and SH, **b** vertical flux of APE, **c** vertical flux of KE, and **d** advection of geopotential height (generation). Units:  $10^{-2} \text{ W/m}^2$



with a value of  $69.8 \times 10^{-2} \text{ W/m}^2$ , is less than 20% that of the climatological magnitude, and the decreasing trend is considerable and reaches the vertical export of APE at 700 hPa, with a value of  $-3.5 \times 10^{-2} \text{ W/m}^2$ . On the other hand, the increasing trend started in the lower layer at 700 hPa, and when compared with the other situations, it had a high rate and reached a maximum value of  $41.1 \times 10^{-2} \text{ W/m}^2$  at 250 hPa, or at the layer with the maximum wind, which is in agreement with the findings by Kung and Baker (1975) and Prezerakos and Michielides (1989). Additionally, this value is more than three times the climatological mean value and more than two times the value during the pre-event stage.

In the post-event stage, as shown by the blue line in Fig. 5b, although the situation tended to have less vertical import of APE at the surface, with a value of  $88.7 \times 10^{-2} \text{ W/m}^2$ , the region above the surface to 600 hPa appeared to have greater vertical import of APE than all other situations. This pattern

was inverted above 600 hPa, where less vertical import of APE occurred than that in the other situations.

**Vertical flux convergence of KE (VKE) ( $-\frac{\partial}{\partial p} \omega K$ )** The climatological mean situation, as shown by the black line in Fig. 5c, showed very low vertically exported KE in the lower atmospheric layers below 700 hPa, which had a value of  $0.0029 \times 10^{-2} \text{ W/m}^2$ . The vertically imported KE increased from 600 hPa, except at 300 hPa, and the maximum value of  $0.126 \times 10^{-2} \text{ W/m}^2$  occurred at 150 hPa.

The situation for the pre-event stage, as shown by the red line in Fig. 5c, showed vertically exported KE in the lower layers below 850 hPa, above which the pattern inverted, yielding vertically imported KE, which reached a maximum value of  $0.295 \times 10^{-2} \text{ W/m}^2$  at 250 hPa.

In the event stage, as shown by the green line in Fig. 5c, throughout the entire atmosphere, KE was vertically imported

into the study area, with a very low magnitude in the lower layers and a maximum value of  $0.18 \times 10^{-2} \text{ W/m}^2$  at 300 hPa.

The vertical flux convergence of KE (VKE) in the post-event stage, as shown by the blue line in Fig. 5c, showed that the atmosphere in the study area had vertically exported KE, with a very low magnitude in the lower layers and increasing magnitudes in the upper layers, reaching a maximum value of  $-0.083 \times 10^{-2} \text{ W/m}^2$  at 300 hPa. However, above 250 hPa, the atmosphere vertically imported KE, which reached a maximum value of  $0.22 \times 10^{-2} \text{ W/m}^2$  at 150 hPa.

**Generation of KE (GKE)** ( $-\left[\nabla \cdot V\Phi + \frac{\partial}{\partial p} \omega\Phi\right]$ ) The climatological profile, as shown by the black line in Fig. 5d, shows a source of KE in the lower layers, with the highest value of  $0.017 \times 10^{-2} \text{ W/m}^2$  at the surface, and the values gradually decreased with height up to 400 hPa and eventually reached negative GKE values, with the lowest value of  $-0.025 \times 10^{-2} \text{ W/m}^2$  at 200 hPa.

In the pre-event stage, as shown by the red line in Fig. 5d, the source of KE is weaker than the climatological mean, with the highest value of  $0.014 \times 10^{-2} \text{ W/m}^2$  at the surface, and the sink is stronger in the layers above 400 hPa, with the lowest value of  $-0.049 \times 10^{-2} \text{ W/m}^2$  at 200 hPa.

In the event stage, as shown by the green line in Fig. 5d, the source of KE in the lower layers is strong, with the highest value at the surface being more than  $0.022 \times 10^{-2} \text{ W/m}^2$ , which is more than 29% higher than the climatological mean value. In contrast, the GKE was less than that of the climatological mean at levels above 500 hPa, reaching a minimum value of  $-0.053 \times 10^{-2} \text{ W/m}^2$  at 200 hPa.

In the post-event stage, as shown by the blue line in Fig. 5d, the profile of GKE coincides with that of the climatological situation, except above 400 hPa, where the GKE is higher than the climatological mean between 400 and 250 hPa and lower than the climatological mean above 250 hPa.

### 3.3.2 Zonal vertical cross section

**Zonal KE (KE) between 30° E and 50° E** In the climatological situation, as shown in Fig. 6a, the maximum meridional average of KE from 25° N to 35° N has a magnitude greater than  $800 \text{ J/m}^2$  at approximately 200 hPa, while the high decreasing rate of KE moves downward to the lower layers.

In the pre-event stage, as shown in Fig. 6b, two areas with patterns that differ from the climatological situation appeared. The western region, with positive differences (corresponding to an increase in KE), had a value larger than  $70 \text{ J/m}^2$  at 250 hPa at approximately 30° E. The eastern region, with negative difference values (corresponding to a decrease in KE), had a difference of  $-30 \text{ J/m}^2$  at 300 hPa at approximately 46° E.

The event stage, as shown in Fig. 6c, features a positive difference, i.e., an increase in KE, with values greater

than  $100 \text{ J/m}^2$  occurring in most of the study area at 300 hPa and centered at approximately 37° E. In addition, the distribution shows that the positive difference continued from high values in the upper levels to  $10 \text{ J/m}^2$  at the surface. Moreover, there were two areas with negative differences. There was a small area in the eastern region between 300 and 400 hPa with a difference of  $-10 \text{ J/m}^2$ , and there was a layer above 150 hPa in the western region with a difference of approximately  $-10 \text{ J/m}^2$ .

In the post-event stage, as shown in Fig. 6d, the core of the maximum positive difference was transferred to the eastern region at 300 hPa and approximately 48° E, and it had a value greater than  $50 \text{ J/m}^2$ . In addition, a negative difference layer was observed above 150 hPa, with a core of  $-10 \text{ J/m}^2$  in the eastern region.

**Zonal RH (Q) between 30° E and 50° E** The climatological distribution of the average meridional RH from 25° N to 35° N (Fig. 6a) shows that the maximum magnitude was found in the lower layers between 36° E and 42° E, with values greater than  $0.44 \text{ W/m}^2$ . The gradient of the vertical distribution rapidly decreased below 850 hPa.

In the pre-event stage, as shown in Fig. 6b, the RH in the lower layer decreased in the western region and increased in the eastern region, and the inverse was found in the upper layers.

In the event stage, as shown in Fig. 6c, the RH in the lower layers was lower than the climatological mean, and the difference was less than  $-0.048 \text{ W/m}^2$ , representing a decrease of approximately 11%. This layer of low RH was thinner in the eastern region, reaching approximately 850 hPa in the east but approximately 300 hPa in the west. In addition, a thin layer of positive values was found at approximately 900 hPa between 30° E and 34° E, with a difference that was greater than  $0.016 \text{ W/m}^2$ . Additionally, a deep layer of positive difference was centered in the eastern region, with a value of  $0.012 \text{ W/m}^2$  between 500 and 400 hPa. The positive core of the RH moved downward from west to east and had maximum core values at approximately 200 hPa in the western region and between 500 and 300 hPa in the eastern region.

In the post-event stage, as shown in Fig. 6d, two thin layers with negative values appeared in the lower layer, and the greatest difference was  $-0.028 \text{ W/m}^2$ . Above these layers, a positive value was found extending from 950 to 850 hPa, with a maximum value of  $0.02 \text{ W/m}^2$ . In addition, above 850 hPa, negative or weak RH differences were found in the central region at approximately 40° E. However, a positive deep layer was found between 46° E and 50° E.

### 3.3.3 Horizontal distribution

**Horizontal flux convergence of KE (HKE)** ( $-\nabla \cdot VK$ ) The climatological distribution of HKE, as shown in Fig. 7a, shows that

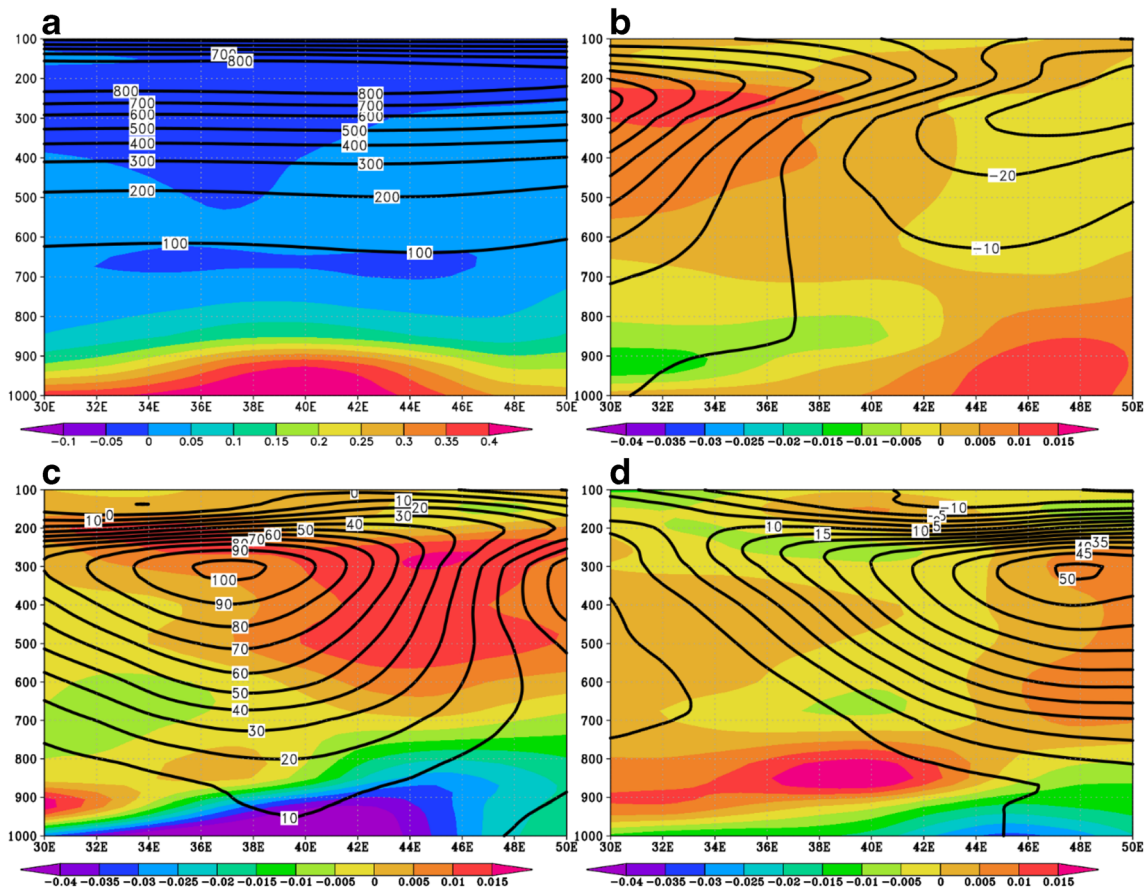


**Fig. 6** Vertical zonal cross sections of the meridional average values between 25° N and 35° N for KE (contours) and RH (shading) in **a** the climatological mean state and the difference between the climatology and

**b** the pre-event, **c** the event, and **d** the post-event stages. Units:  $J/m^2$  for KE and  $W/m^2$  for RH

KE was exported from eastern Africa to the surrounding area, with the highest value of  $-0.2 W/m^2$  located over Sudan. KE was imported to the northern AP, Levant and Turkey from the surrounding areas, with the highest value of  $0.3 W/m^2$  located over Iraq. Furthermore, KE was exported from the southeastern AP, Iran and Pakistan to the surrounding areas, with the highest value of  $-0.4 W/m^2$  located over Pakistan.

In the pre-event stage, as shown in Fig. 7b, the exported KE in eastern Africa was converted to imported KE, while the imported KE over the northwestern AP, Levant and Turkey increased. Furthermore, the imported KE in the northeastern AP decreased by more than  $-0.2 W/m^2$ , while the exported KE in the southern AP increased by more than  $-0.1 W/m^2$ .

As shown in Fig. 7c, the exported KE over eastern Africa and the Mediterranean in the climatological situation increased by more than  $-0.3 W/m^2$  in the event stage, and the imported KE over the AP, Levant and Turkey increased by more than  $0.6 W/m^2$ . In addition, the exported KE over the southeastern AP, Iran and Pakistan increased, with a value of approximately  $-0.2 W/m^2$  over Pakistan.

In the post-event stage, as shown in Fig. 7d, the exported KE over eastern Africa and the eastern Mediterranean

increased by approximately  $-0.2 W/m^2$ , while the imported KE over the northwestern AP, Levant and Turkey decreased by approximately  $-0.2 W/m^2$ . The imported KE over the northeastern AP increased by approximately  $0.2 W/m^2$ , and the exported KE over the southeastern AP, Iran and Pakistan decreased by more than  $0.1 W/m^2$ .

**Horizontal flux convergence of APE (HPE) ( $-\nabla \cdot VA$ )** The climatological distribution of the horizontal flux convergence of APE (HPE) in the layer between 1000 and 100 hPa, as shown in Fig. 7a, shows that a sequence of imported and exported APE extended from the tropical African region to the AP and northern Iran. The imported APE over the AP was surrounded by two areas of exported APE, one over the Red Sea, which was adjacent to the western AP, and the other over the Arabian Gulf, which was adjacent to the eastern area of the AP. Eastern Africa, the northern AP and the Levant had imported APE, which may explain why the atmosphere in these regions is baroclinic, as described by Smith (1980).

In the pre-event stage, as shown in Fig. 7b, the imported APE over the AP increased. In addition, the exported APE increased over the Red Sea but decreased over the Arabian

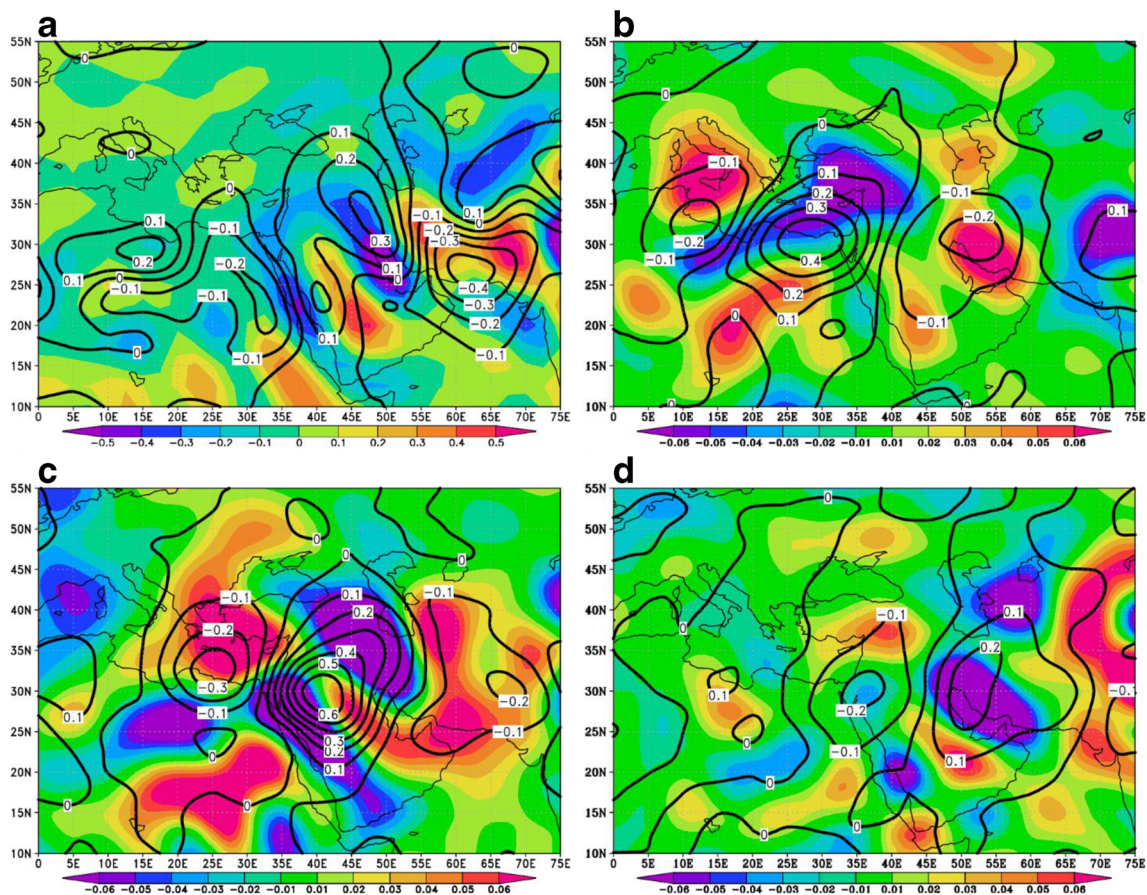


**Fig. 7** Horizontal distribution of vertical average values in the layer between 1000 and 100 hPa for KE (contour) and APE (shaded) in **a** the climatological mean state and the difference between the climatology and **b** the pre-event, **c** the event, and **d** the post-event stages. Units:  $W/m^2$

Gulf and adjacent areas. Moreover, the imported APE increased over northern Africa, the Mediterranean, the northern AP, and Levant but decreased over the Saharan region.

In the event stage, as shown in Fig. 7c, two inverse sequences of HPE differences occurred. The northern region experienced an increase in the exported APE over Africa and a decrease in the exported APE over the eastern Mediterranean and Levant. The southern region experienced an increase in the imported APE over Africa and an increase in the exported APE over the Red Sea, western AP, Arabian Gulf, and eastern AP. In addition, a small area of imported APE was found over the central AP. One of the most important features of this stage was that the difference retained the pattern of export and import of APE in the climatological series; however, the exported APE was enhanced, especially over the study area. These features may explain the tropical midlatitude interactions that produced the eastward shift in KE and synoptic systems, as indicated by Raju et al. (2011).

In the post-event stage, as shown in Fig. 7d, the southern sequence of the event stage was still found, but it was present in a weak form and was shifted to the southwest, while the northern sequence became very weak and was shifted eastward.

## 4 Discussion and conclusions

In this study, the observations of dust/sand storms and severe dust/sand storms were considered together as dust storm cases. The distributions of the numbers of observed dust storms demonstrated that most of the stations had fewer observations than the mean number of observations. In addition, the stations with high numbers of observed dust storms were located in the eastern region, i.e., close to the Syrian and Iraq deserts. Moreover, the total monthly average of the number of observed dust storms demonstrated that the number doubled from March, a relatively cold month, to May, a relatively warm month. The trends in the annual distribution of dust storms indicated that the study period could be divided into two periods: from 1978 to 1994, with a high rate of increase, and from 1995 to 2008, with a low rate of decrease.

The climatology of the synoptic features, which is used as the background for describing the atmospheric conditions of the dust event stages, demonstrated that the AP was influenced by a southern low-pressure cell that has two troughs over the Arabian Gulf and the Red Sea. However, the Saharan region was influenced by a pronounced pressure gradient that extended from west to east across the entire Sahara.

In addition, the Azores High and the troughs over the AP formed an area with a high-pressure gradient over the Levant and northwestern AP.

Generally, the interaction of the MSLP in various atmospheric systems formed a zonal area with a high-pressure gradient that extended from west to east over northern Africa in the pre-event stage, which could explain the northward transport of dust from the Saharan region, as described by Barkan and Alpert (2010). This area with a high-pressure gradient was oriented meridionally over the eastern Mediterranean region in the event stage and could explain the eastward transport of dust from Africa to Asia, as described in Awad and Mashat (2014b) and Prakash et al. (2015). This area with a high-pressure gradient then diminished in the post-event stage, as shown by the results of decreasing KE based on the generation of KE. Additionally, the distribution of pressure over the AP showed increasing pressure and stability in the pre-event stage and decreasing pressure and stability in the event stage, which is in agreement with the results from Karyampudi et al. (1999).

In the upper atmospheric levels, the AP was influenced by pronounced geopotential gradients from the west, east, and north. In addition, the northern cyclone affected the northern AP by a trough, while the subtropical anticyclone affected eastern Africa. Furthermore, these atmospheric systems were stronger in the pre-event stage than the climatological mean, thereby producing a high geopotential gradient and a strong anticyclonic wind pattern, which is in agreement with the spring dust situation described by Barkan and Alpert (2008). This change reached its maximum strength in the event stage, and it weakened after the dust storms passed over the region, which confirmed the importance of the role of the pressure gradient in dust events, as found by Barkan and Alpert (2010) and Awad and Mashat (2014a). The trough of the northern cyclone directly influenced the northern AP, becoming less stable in the event stage and more stable in the post-event stage, which is in agreement with the findings of Hsu et al. (1999).

The temperature distribution demonstrated a ridge of high temperature over the northern AP, which is in agreement with the temperature conditions of the spring dust Barkan and Alpert (2008). This ridge formed a strip of area with a temperature gradient around the AP, especially in the Saharan and Mediterranean regions. This feature has been cited by Qian et al. (2002) as a factor responsible for increasing the frequency of dust events, and by Nasrallah et al. (2004) as a factor responsible for generating dust over the AP. Furthermore, a strip of area with low stability extended from west to east over the southern Mediterranean and northern AP, with a southern extension over the AP. In addition, a high-stability gradient area formed over the western/eastern AP, Levant, and northern

Sahara. Obviously, the temperature distribution shows the importance of the northward transport of tropical heat to the northern AP and the importance of the temperature gradient on the distribution of regional stability and the flux convergence of APE. Additionally, APE was generated in tropical regions and transported to the study area through a series of areas exporting and importing APE. This process was enhanced in the event stage but was disrupted in the pre- and post-event stages. Moreover, this process of tropical heat transport was considered a factor in the generation of Saharan dust events by Abdel Basset (2001).

The development of the atmospheric wind indicated that the development of the anticyclonic wind pattern shifted northward from its location in the climatological situation to the northern AP and Iraq in the pre-event stage, which formed a northerly (shamal) wind over Iraq and the eastern AP; this process represents one of the dust generation factors in this region (Barkan and Alpert 2008; Hamidi et al. 2013; Houssos et al. 2015; Shalaby et al. 2015; Yu et al. 2016; Kaskaoutis et al. 2017). In association with these developments, the wind pattern over the AP changed from an anticyclonic wind pattern in the pre-event stage to a very strong cyclonic wind pattern in the event stage to a weak cyclonic and easterly wind pattern in the post-event stage, as shown by Hamidi et al. (2013). Additionally, the core of the jet stream intensified and shifted southward in the event stage compared with the intensity and position in the pre-event stage and only the intensity in the post-event stage, which was different from the results from non-storm dust, as studied by Awad and Mashat (2016a); however, Hamidi et al. (2013) found that it was necessary to produce the cyclonic wind pattern or frontal system that accompanies the dust storm.

The energy analysis shows that the conversion of SH into KE in the study area in the event stage was many times greater than that in the climatological situation, whereas the conversion was weak in the pre-event stage and inverted in the post-event stage. Furthermore, the profile data show that the maximum conversion of SH in the event stage occurs in the upper level close to the expected level of the dust cloud (Alpert and Ganor 1993; Duce 1995; Prospero 1996; Alpert et al. 2004b), while the maximum conversion in the other stages occurs at the surface.

The vertical distribution of the flux convergence of APE indicated that the atmosphere in the study area tends to receive (import) less APE in the dust event stage than in the climatological situation or the other event stages. Moreover, a loss (export) of APE occurs at approximately 700 hPa. However, there is more imported APE in dust events above 600 hPa in the event stage than in the other stages, with the maximum import occurring at 250 hPa, i.e., close to the level of the maximum wind. This atmospheric behavior is inverted after the dust event passes, and the lower layer below 600 hPa imports more APE and the upper layer imports less APE.

The vertical flux convergence of KE demonstrated that more KE is imported in the deep atmospheric layer in the pre-event stage than in the climatological situation, which means that KE is transferred from the upper layers. This transfer increased in the event stage. In contrast, in the post-event stage, the process is reversed, and KE is exported throughout most of the atmosphere, which agrees with the processes observed in Mediterranean cyclones by Wahab and Abdel Basset (2000).

The vertical distribution of the flux convergence of APE and KE demonstrated that the combination of high wind speeds and less vertically imported APE in the upper layer is comparable to the combination of low wind speeds and high vertically imported APE in the lower layer, i.e., the vertical flux convergences of KE and APE compensate for each other.

Furthermore, compared with the pattern in the climatological situation, the vertical profile of GKE indicated that the source of KE decreased in the lower layer before the event stage and increased in the event stage. In contrast, the KE sink in the upper layers in the event stage was more than that in the pre-event stage and the climatological situation, which agrees with the results by Wahab and Abdel Basset (2000) for the development of the Mediterranean cyclone.

Clearly, the previous discussion of the vertical profiles shows that the main sources of KE are the vertically imported KE and the conversion of SH into KE, while the main sink of KE is produced by the decreasing geopotential gradient, as demonstrated by the GKE terms. Furthermore, the discussion indicated that in the event stage, the APE increased above 600 hPa but decreased below this pressure level, which reflected the effect of dust clouds on the atmosphere, as observed by Kishcha et al. (2003). In the case of dust storms, the lower layers are cooled, while the upper layers are warmed.

The zonal distribution of the meridional average of KE shows that the location of the maximum positive difference in KE between a dust storm event and the climatological situation migrated from the west in the pre-event stage to the east in the post-event stage. In addition, the difference reached its highest positive value of  $100 \text{ J/m}^2$  in the event stage. Furthermore, the distribution of different values shows a deep transfer of KE in the event stage, which is not as clear in the other stages. This KE distribution confirmed the distribution of the maximum wind and its maximum effect on the study area in the event stage.

The energy processes and the change in the jet stream in the dust stages indicated that the atmosphere in the event stage is more integrated than that in the other stages. In other words, in the event stage, there is good communication between atmospheric layers.

The distribution of the RH differences indicated that the decrease in RH started from the western region in the pre-event stage and spread to the entire region in the event stage. A layer of positive RH differences formed in the event stage,

and this positive layer intensified and became thinner in the post-event stage. Additionally, the RH difference had a high gradient in the lower layers in the event stage, which confirmed the existence of cooling beneath the dust storm cloud, as observed by Kishcha et al. (2005).

The horizontal distribution of the flux convergence terms showed that the exported KE during the dust event moved from the western side to the whole area and the eastern side of the northern AP, Levant, and Turkey as the dust storm progressed from the pre- to post-event stages. This result indicates that the KE in the region increased as the event developed and decreased as the event decayed. These increases and decreases occurred through the import and export of KE from the surrounding areas, as described by Wahab and Abdel Basset (2000).

Generally, the results of this study identified the similarities between the energy characteristics of the event stages and those of the climatological mean state, which means that the regional climate is highly influenced by the characteristics of the dust storms affecting the region.

**Acknowledgments** The authors thank the DSR for technical and financial support. The authors also acknowledge the National Centers for Environmental Prediction (NCEP) and the National Center for Atmospheric Research (NCAR) for providing meteorological data.

**Funding information** This study was funded by the Deanship of Scientific Research (DSR) at King Abdulaziz University, under grant no. G: 165-155-1439.

## Compliance with ethical standards

**Conflict of interest** The authors declare that they have no conflict of interest.

## References

- Abdel Wahab M, Abdel Basset H (2000) Energy exchanges for Mediterranean weather systems. *Meteorog Atmos Phys* 73:1–23
- Abdel Basset H (2001) Energy conversion of a desert depression. *Meteorog Atmos Phys* 76:203–222. <https://doi.org/10.1007/s007030170030>
- Al-Jumaily KJ, Ibrahim MK (2013) Analysis of synoptic situation for dust storms in Iraq. *Int J Energy Environ* 4–5:851–858
- Alpert P, Ganor E (1993) A jet stream associated heavy dust storm in the western Mediterranean. *J Geophys Res* 98(D4):7339–7349
- Alpert P, Osetinsky I, Ziv B, Shafir H (2004a) Semi-objective classification for daily synoptic systems: application to the eastern Mediterranean climate change. *Int J Climatol* 24:1001–1011
- Alpert P, Kishcha P, Shtivelman A, Krichak SO, Joseph JH (2004b) Vertical distribution of Saharan dust based on 2.5 year model predictions. *Atmos Res* 70:109–130
- Amanollahi J, Kaboodvandpour S, Qhavami S, Mohammadi B (2015) Effect of the temperature variation between Mediterranean Sea and Syrian deserts on the dust storm occurrence in the western half of Iran. *Atmos Res* 154:116–125
- Awad A, Mashat A (2014a) The synoptic patterns associated with spring widespread dusty days in central and eastern Saudi Arabia. *Atmos* 5(4):889–913

- Awad AM, Mashat AS (2014b) Synoptic features associated with dust transition processes from North Africa to Asia. *Arab J Geosci* 7(6): 2451–2467. <https://doi.org/10.1007/s12517-013-0923-4>
- Awad AM, Mashat AWS (2016a) Synoptic characteristics of spring dust days over northern Saudi Arabia. *Air Qual Atmos Health* 9(1):41–50
- Awad AM, Almazroui M (2016b) Climatology of the winter Red Sea Trough. *Atmos Res* 182(2016):20–29. <https://doi.org/10.1016/j.atmosres.2016.07.019>
- Awad AM, Mashat AWS (2018) Climatology of the autumn Red Sea trough. *Theor Appl Climatol*. <https://doi.org/10.1007/s00704-018-2453-1>
- Barkan J, Alpert P (2008) Synoptic patterns associated with dusty and non-dusty seasons in the Sahara. *Theor Appl Climatol* 94:153–162. <https://doi.org/10.1007/s00704-007-0354-9>
- Barkan J, Alpert P (2010) Synoptic analysis of a rare event of Saharan dust reaching the Arctic region. *Weather* 65:208–211
- De Vries AJ, Tyrlis E, Edry D, Krichak SO, Steil B, Lelieveld J (2013) Extreme precipitation events in the Middle East: dynamics of the active Red Sea trough. *J Geophys Res Atmos* 118:7087–7108. <https://doi.org/10.1002/jgrd.50569>
- Duce RA (1995) Sources, distributions and fluxes of mineral aerosols and their relationship to climate. In: Charlson RJ, Heintzenberg JJ (eds) *Aerosol forcing and climate*, pp 43–72
- Danard MB (1966) On the contribution of released latent heat to changes in available potential energy. *Ibid*. 5:81–84
- Engelstaedter S, Tegen I, Washington R (2006) North African dust emissions and transport. *Earth Sci Rev* 79:73–100
- Ganor E, Stupp A, Osetinsky I, Alpert P (2010) Synoptic classification of lower troposphere profiles for dust days. *J Geophys Res* 115:1–8
- Gates WL (1961) Static stability in the atmosphere. *J Meteor* 18:526–533
- Ginoux P, Prospero JM, Torres O, Chin M (2004) Long-term simulation of global dust distribution with the GOCART model: correlation with North Atlantic oscillation. *Environ Model Softw* 19:113–128
- Ginoux P, Prospero JM, Gill TE, Hsu NC, Zhao M (2012) Global-scale attribution of anthropogenic and natural dust sources and their emission rates based on MODIS Deep Blue aerosol products. *Rev Geophys* 50:RG3005. <https://doi.org/10.1029/2012RG000388>
- Gkikas A, Houssos EE, Hatzianastassiou N, Papadimas CD, Bartzokas A (2012) Synoptic conditions favouring the occurrence of aerosol episodes over the broader Mediterranean basin. *Q J Roy Meteorol Soc* 138:932–949
- Goudie A, Middleton N (2006) *Desert dust in the global system*. Springer, Heidelberg
- Hamidi M, Kavianpour MR, Shao Y (2013) Synoptic analysis of dust storms in the Middle East. *Asia-Pac J Atmos Sci* 49:279–286
- Hamidi M (2019) Atmospheric investigation of frontal dust storms in southwest Asia. *Asia-Pacific J Atmos Sci* 55:177. <https://doi.org/10.1007/s13143-018-0083-2>
- Hannachi A, Awad A, Ammar K (2011) Climatology and classification of spring Saharan cyclone tracks. *ClimDyn* 37:473–491
- Houssos EE, Chronis T, Fotiadi A, Hossain F (2015) Atmospheric circulation characteristics favoring dust outbreaks over the Solar Village, Central Saudi Arabia. *Mon Weather Rev* 143:3263–3275
- Hsu NC, Herman JR, Torres O, Holben BN, Tanre D, Eck TF, Smimov A, Chatenet B, Lavenu F (1999) Comparisons of the TOMS aerosol index with Sunphotometer aerosol optical thickness: results and applications. *J Geophys Res* 104:6269–6279
- Kalnay E, Kanamitsu M, Kistler R, Collins W, Deaven D, Gandin L, Iridell M, Saha S, White G, Woollen J, Zhu Y, Chelliah M, Ebisuzaki W, Higgins W, Janowiak J, Mo KC, Ropolewski C, Wang J, Leetma A, Reynolds R, Jenne R, Joseph D (1996) The NCEP/NCAR 40-year Reanalysis project. *Bull Am Meteorol Soc* 77:437–471
- Karyampudi VM, Palm SP, Reagen JA, Hui F, Grant WB, Hoff RM, Mouline HR, Pierce HF, Torres O, Browell ED, Melfi SH (1999) Validation of the Saharan dust plume conceptual model using lidar, Meteosat, and ECMWF data. *Bull Am Meteorol Soc* 80:1045–1075
- Kaskaoutis DG, Kambezidis HD, Nastos PT, Kosmopoulos PG (2008) Study on an intense dust storm over Greece. *Atmos Environ* 42(29): 6884–6896
- Kaskaoutis DG, Houssos EE, Rashki A, Francois P, Legrand M, Goto D, Bartzokas A, Kambezidis HD, Takemura T (2016) The Caspian Sea – Hindu Kush index (CasHKI): a regulatory factor for dust activity over Southwest Asia. *Glob Planet Chang* 137:10–23
- Kaskaoutis DG, Rashki A, Houssos EE, Legrand M, Francois P, Bartzokas A, Kambezidis HD, Dumka UC, Goto D, Takemura T (2017) Assessment of changes in atmospheric dynamics and dust activity over Southwest Asia using the Caspian Sea–Hindu Kush index. *Int J Climatol* 37(Suppl.1):1013–1034
- Kishcha P, Alpert P, Barkan J, Kirchner I, Machenhauer B (2003) Atmospheric response to Saharan dust deduced from ECMWF reanalysis (ERA) temperature increments. *Tellus B* 55:901–913
- Kistler R, Collins W, Saha S, White G, Woollen J, Kalnay E, Chelliah M, Ebisuzaki W, Kanamitsu M, Kousky V, vandenDool H, Jenne R, Fiorino M (2001) The NCEP/NCAR 50-year Reanalyses: Monthly CD-ROM and documentation. *Bull Am Meteorol Soc* 82: 247–267
- Kung EC (1966) Kinetic energy generation and dissipation in the large-scale atmospheric circulation. *Mon Weather Rev* 94(2):67–82
- Kung EC, Baker WE (1975) Energy transformations in middle latitudes. *Q J Roy Meteorol Soc* 101:793–815
- Lorenz EN (1955) Available potential energy and the maintenance of the general circulation. *Tellus* 7:157–167
- Margules M (1903) Ober die Energie der St.irme. *Jahrb. Zentrhnst. Meteorol.* 1–26. (Translation by C. Abbe (1910) in *Smithsonian Institution Miscellaneowr Collection* 51, 553–595.)
- Mashat A, Awad AM (2010) The classification of the dusty areas over the Middle-East. *Bull FacSci, Cairo Univ* 78(A):1–19
- Middleton NJ (1986) Dust storms in the Middle East. *J Arid Environ* 10: 83–96
- Mohalifi S, Bedi HS, Krishnamurti TN, Cocke SD (1998) Impact of shortwave effects on the summer season heat low over Saudi Arabia. *Mon Weather Rev* 126:3153–3168
- Nasrallah HA, Nieplova E, Ramadan E (2004) Warm season extreme temperature events in Kuwait. *J Arid Environ* 56:357–371
- Natsagdory L, Jugder D, Chung YS (2003) Analysis of dust storms observed in Mongolia during 1937–1999. *Atmos Environ* 37:1401–1411
- Notaro M, Alkolibi F, Fadda E, Bakhrijy F (2013) Trajectory analysis of Saudi Arabian dust storms. *J Geophys Res Atmos* 118:6028–6043. <https://doi.org/10.1002/jgrd.50346>
- Pease PP, Tchakerian VP, Tindale NW (1998) Aerosols over the Arabian Sea: geochemistry and source areas for aeolian desert dust. *J Arid Environ* 39:477–496
- Prakash PJ, Stenchikov G, Kalenderski S, Osipov S, Bangalath H (2015) The impact of dust storms on the Arabian Peninsula and the Red Sea. *Atmos Chem Phys* 15(1):199–222. <https://doi.org/10.5194/acp-15-199-2015>
- Prezerakos NG, Michaclides SC (1989) A composite diagnosis in sigma coordinates of the atmospheric energy balance during intense cyclonic activity. *Quart J Roy Meteor Soc* 115:463–486
- Prospero JM (1996) In: Guerzoni S, Chester R (eds) *Saharan dust transport over the North Atlantic Ocean and Mediterranean: an overview, in The impact of desert dust across the Mediterranean*. Kluwer Acad., Norwell, pp 133–151
- Prospero JM, Ginoux P, Torres O, Nicholson SE, Gill TE (2002) Environmental characterization of global sources of atmospheric soil dust identified with the Nimbus 7 Total Ozone Mapping Spectrometer (TOMS) absorbing aerosol product. *Rev Geophys* 40:1002. <https://doi.org/10.1029/2000RG000095>
- Raispour K, Khosravi M, Tavousi T, Sharifikiya M (2014) The influence of the polar front jet stream on the formation of dust events in the

- southwest of Iran. *AirQualAtmos Health* 9:15–23. <https://doi.org/10.1007/s11869-014-0270-y>
- Raju PVS, Bhatla R, Mohanty UC (2011) A study on certain aspects of kinetic energy associated with western disturbances over Northwest India. *Atmósfera* 24(4):375–384
- Rashki A, Kaskaoutis DG, Rautenbach CJW, Flamant C, Abdi VF (2014) Spatio-temporal variability of dust aerosols over the Sistan region in Iran based on satellite observations. *Nat Hazards* 71:563–585
- Raziei T, Mofidi A, Santos AJ, Bordi I (2012) Spatial patterns and regimes of daily precipitation in Iran in relation to large-scale atmospheric circulation. *Int J Climatol* 32:1226–1237
- Qian W, Quan L, Shi S (2002) Variability of the dust storm in China and its climatic control. *J Clim* 15:1216–1229
- Shalaby A, Rappenglueck B, Eltahir EAB (2015) The climatology of dust aerosol over the Arabian Peninsula. *Atmospher Chem Phys Dis* 15(2):1523–1571
- Chen T-C, Lee Y-H (1983) A study of the kinetic energy generation with general circulation model. *J Meteor Soc* 61:439–448
- Smirnov A, Holben BN, Dubovic O, O'Neill NT, Eck TF, Westphal DL, Goroth AK, Pietras C, Slutsker I (2002) Atmospheric aerosol optical properties in the Persian Gulf. *J Atmos Sci* 59:620–634
- Smith PJ (1969) On the contribution of a limited region to the global energy budget. *Tellus* 21:202–207
- Smith PJ, Horn LH (1969) A computational study of the energetics of a limited region of the atmosphere. *Tellus* 21:193–201
- Smith PJ (1980) The energetics of extratropical cyclones. *Rev Geophys* 18:378–386
- Vishkaee FA, Flamant C, Cuesta J et al (2011) Multiplatform observations of dust vertical distribution during transport over Northwest Iran in the summertime. *J Geophys Res* 116:D05206. <https://doi.org/10.1029/2010JD014573>
- Washington R, Todd M, Middleton NJ, Goudie AS (2003) Dust-storm source areas determined by the total ozone monitoring spectrometer and surface observations. *Ann Assoc Am Geogr* 93:297–313. <https://doi.org/10.1111/1467-8306.9302003>
- Washington R, Todd MC (2005) Atmospheric controls on mineral dust emission from the Bodele depression, Chad: the role of the low level jet. *Geophys Res Lett* 32(17):L17701 ISSN 0094–8276
- WMO (2005) Climate and land degradation. Geneva, Switzerland, World Meteorological Organization
- Yu Y, Notaro M, Liu Z, Kalashnikova O, Alkolibi F, Fadda E, Bakhrjy F (2013) Assessing temporal and spatial variations in atmospheric dust over Saudi Arabia through satellite, radiometric, and station data. *J Geophys Res* 118:1–12. <https://doi.org/10.1002/2013JD020677>
- Yu Y, Notaro M, Kalashnikova OV, Garay MJ (2016) Climatology of summer Shamal wind in the Middle East. *J Geophys Res-Atmos* 121:289–305. <https://doi.org/10.1002/2015JD024063>

**Publisher's note** Springer Nature remains neutral with regard to jurisdictional claims in published maps and institutional affiliations.